

# Measuring spectroscopy and magnetism of extracted and intracellular magnetosomes using soft X-ray ptychography

Xiaohui Zhu<sup>a</sup>, Adam P. Hitchcock<sup>a,1</sup>, Dennis A. Bazylinski<sup>b</sup>, Peter Denes<sup>c</sup>, John Joseph<sup>d</sup>, Ulysses Lins<sup>e</sup>, Stefano Marchesini<sup>c</sup>, Hung-Wei Shiu<sup>c,f</sup>, Tolek Tyliczszak<sup>c</sup>, and David A. Shapiro<sup>c</sup>

<sup>a</sup>Department of Chemistry and Chemical Biology, McMaster University, Hamilton, ON, Canada L8S 4M1; <sup>b</sup>School of Life Sciences, University of Nevada at Las Vegas, Las Vegas, NV 89154; <sup>c</sup>Advanced Light Source, Lawrence Berkeley National Laboratory, Berkeley, CA 94720; <sup>d</sup>Engineering Division, Lawrence Berkeley National Laboratory, Berkeley, CA 94720; <sup>e</sup>Instituto de Microbiologia, Universidade Federal do Rio de Janeiro, Rio de Janeiro, RJ 2194-590, Brazil; and <sup>f</sup>National Synchrotron Radiation Research Center, Hsinchu, Taiwan 30076, Republic of China

Edited by Stephen P. Cramer, University of California, Davis, CA, and accepted by Editorial Board Member John W. Sedat November 15, 2016 (received for review June 24, 2016)

**Characterizing the chemistry and magnetism of magnetotactic bacteria (MTB) is an important aspect of understanding the biomineralization mechanism and function of the chains of magnetosomes (Fe<sub>3</sub>O<sub>4</sub> nanoparticles) found in such species. Images and X-ray absorption spectra (XAS) of magnetosomes extracted from, and magnetosomes in, whole *Magnetovibrio blakemorei* strain MV-1 cells have been recorded using soft X-ray ptychography at the Fe 2p edge. A spatial resolution of 7 nm is demonstrated. Precursor-like and immature magnetosome phases in a whole MV-1 cell were visualized, and their Fe 2p spectra were measured. Based on these results, a model for the pathway of magnetosome biomineralization for MV-1 is proposed. Fe 2p X-ray magnetic circular dichroism (XMCD) spectra have been derived from ptychography image sequences recorded using left and right circular polarization. The shape of the XAS and XMCD signals in the ptychographic absorption spectra of both sample types is identical to the shape and signals measured with conventional bright-field scanning transmission X-ray microscope. A weaker and inverted XMCD signal was observed in the ptychographic phase spectra of the extracted magnetosomes. The XMCD ptychographic phase spectrum of the intracellular magnetosomes differed from the ptychographic phase spectrum of the extracted magnetosomes. These results demonstrate that spectro-ptychography offers a superior means of characterizing the chemical and magnetic properties of MTB at the individual magnetosome level.**

ptychography | magnetotactic bacteria | biomineralization | STXM | XAS-XMCD

Microorganisms have long been thought to play crucial roles in ecosystems because they are actively involved in the global cycles of principal elements necessary to life, such as C, O, N, P, S, and Fe (1, 2). These living organisms selectively take up certain elements from the local environment, transform their chemical state, and synthesize minerals inside or outside the cells under strict biochemical and genetic control, a process known as biomineralization. To date, over 60 different minerals of biological origin have been identified (3). One of the most fascinating examples of biomineralization is the formation of single-domain magnetic nanocrystals, termed magnetosomes, within magnetotactic bacteria (MTB) (4, 5). The magnetosomes, made of magnetite (and, less commonly, greigite), are surrounded by lipid membranes and organized in chains inside MTB. The chain of magnetically aligned magnetosomes imparts a sufficiently large magnetic moment to the cells so that they are spatially oriented by the magnetic interaction with the Earth's geomagnetic field (4, 5). This alignment, coupled with chemical aerotaxis, is believed to help MTB locate and maintain position at the oxic/anoxic transition zone, their preferred habitat. Ferromagnetic particles have also been found in other organisms, such as algae (6), fish (7), insects (8), birds (9), and even humans (10). As one of the simplest

biomineralizing microorganisms, MTB serve as a useful model for understanding the evolution and mechanism of biomineralization (4, 5, 11, 12). In addition, they provide an easily accessible system to study the significance of biomagnetism for detection and use of the local Earth's magnetic field in other living organisms.

Imaging and quantifying magnetic properties of MTB have been achieved with several techniques, including superconducting quantum interference device (SQUID) magnetometry (13), magnetic force microscopy (MFM) (14), and electron holography in transmission electron microscopy (TEM) (15). However, SQUID microscopy only provides the integral properties of ensembles of magnetic particles, whereas the magnetic characterization of individual particles is still inaccessible (16). MFM has a spatial resolution of better than 10 nm, but the direct extraction of quantitative information from MFM images is challenging (17). Although electron holography in TEM provides quantitative information about the magnetic structure of individual magnetosomes with high spatial resolution (18), radiation damage and the strict requirement for sample thickness (less than 50 nm) limit its application. In addition, the presence of the magnetic field in electron holography might influence the internal magnetic structure of MTB, and there is no element or site specificity. In this

## Significance

**Magnetotactic bacteria are one of the simplest systems that perform biomineralization: organisms that create inorganic materials using biochemistry under genetic control. They synthesize magnetosomes, which are intracellular, membrane-bound nanoscale single crystals of magnetite, a magnetic iron oxide. We studied the magnetism of individual magnetosomes inside individual cells with spectro-ptychography, a new technique of high-resolution X-ray microscopy. Our results help us to understand how the cells biomineralize magnetosomes and their function in the cell ecophysiology. In addition to demonstrating a large improvement in spatial resolution relative to earlier nonptychography studies, the results presented provide insights into magnetosome biomineralization.**

Author contributions: A.P.H. designed research; X.Z., A.P.H., H.-W.S., T.T., and D.A.S. performed research; D.A.B., P.D., J.J., U.L., S.M., T.T., and D.A.S. contributed new reagents/analytic tools; X.Z. and A.P.H. analyzed data; X.Z., A.P.H., and D.A.B. wrote the paper; P.D. and J.J. developed instrumentation (fast camera); S.M. developed ptychography reconstruction software; H.-W.S. developed software; T.T. developed microscope acquisition software; and D.A.S. developed analysis software.

The authors declare no conflict of interest.

This article is a PNAS Direct Submission. S.P.C. is a Guest Editor invited by the Editorial Board.

<sup>1</sup>To whom correspondence should be addressed. Email: aph@mcmaster.ca.

This article contains supporting information online at [www.pnas.org/lookup/suppl/doi:10.1073/pnas.1610260114/-DCSupplemental](http://www.pnas.org/lookup/suppl/doi:10.1073/pnas.1610260114/-DCSupplemental).

context, synchrotron-based soft X-ray spectromicroscopy, which detects the intrinsic magnetism of a sample through the X-ray magnetic circular dichroism (XMCD) effect (19), is an ideal tool to probe valence state, site occupancy, and element-specific magnetic moments in biologically generated magnetic structures with nanoscale spatial resolution (19, 20).

XMCD is the difference of X-ray absorption spectra (XAS) recorded with circularly polarized X-rays parallel and antiparallel to the magnetization direction. XMCD measured with a scanning transmission X-ray microscope (STXM) has been successfully applied as a tool to study the chemistry, magnetism, and biomineralization mechanism of MTB on an individual magnetosome basis (21–23). STXM-XMCD has also been used to probe the magnetic and chemical properties of extracellular magnetic iron oxides produced by bacteria (24). However, the spatial resolution of current STXMs is typically  $\sim 30$  nm when generated by a 25-nm outer zone, Fresnel zone plate (ZP), and the monochromaticity and lateral coherence of the X-rays are such that the spot size is diffraction-limited. This resolution is just sufficient to resolve and measure the XMCD of individual magnetosomes (21–23), but the size, morphology, and orientation of magnetosomes are not well resolved, which makes extraction of spectral information difficult.

Ptychography is a coherent diffractive imaging technique (25). In ptychography, coherent scattering patterns are measured from an array of spots in a region of interest (ROI). When the spots are chosen with sufficient overlap, the set of measured elastic scattering patterns can be reduced reliably to the amplitude (modulus) and phase information of the object's transmission, as well as an illumination probe function (25, 26). Unlike conventional lens-based microscopic imaging techniques, such as STXM, ptychography is not limited by the properties of the X-ray optics used, has the potential to reach near atomic-scale spatial resolution with very short-wavelength X-rays (27), and can image with Rayleigh wavelength-limited resolution in the soft X-ray region (at the Fe  $L_{2,3}$  edge, the wavelength is 1.8 nm). Ptychography has been used to image biological cells (28, 29), labyrinthine domains in magnetic multilayers (30), and 3D structure with 16-nm spatial resolution (31). Recently, soft X-ray spectro-ptychography was developed at the Advanced Light Source (32–35), which opens up the possibility of chemical speciation via X-ray spectroscopy with spatial resolution of a few nanometers. Here, we present the application of spectro-ptychography to measure X-ray absorption and XMCD spectra at the Fe  $L_{2,3}$  edge to study spatially resolved chemistry and magnetism of magnetosomes extracted from cells and inside whole MTB cells. A preliminary report of some of these results has been presented elsewhere (36).

## Results

**Fe 2p Spectro-ptychography Study of Extracted Magnetosomes.** Fig. 1A shows the ptychography modulus (amplitude) image of a set of chains of magnetosomes extracted from *Magnetovibrio blakemorei* strain MV-1 cells using the procedure described by Alphandéry et al. (37). This image was measured with a ZP with a 60-nm outer zone width, and thus a 72-nm diffraction-limited spot size. Fig. S1 presents the conventional bright-field STXM image of a larger region of the same sample, which includes the area imaged by ptychography, recorded using the same ZP. In that image (Fig. S1), only the outline of magnetosome chains could be identified. In contrast, the individual magnetosomes are spatially well resolved with ptychography using the same ZP (Fig. 1A). Fig. S2A shows a conventional STXM image of magnetosome chains using a higher resolution ZP, one with a 25-nm outer zone width. Although the magnetosomes are better resolved, the achieved spatial resolution (31 nm diffraction-limited) is significantly worse than the spatial resolution that was achieved with ptychography using a 60-nm ZP, as can be seen by a direct comparison with an expanded-scale ptychography modulus image

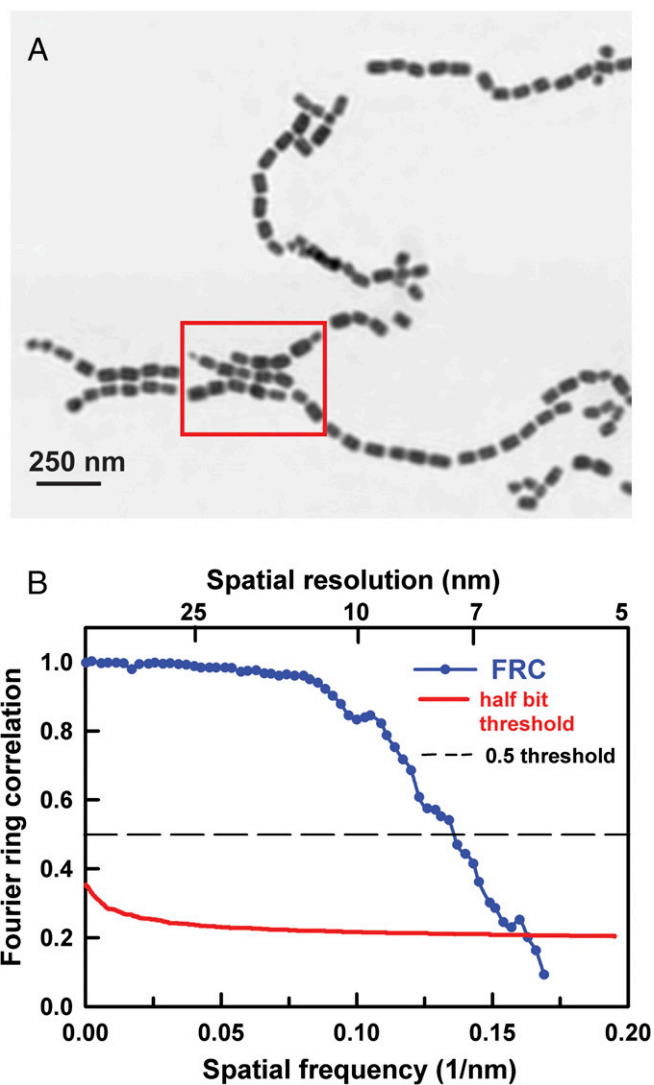


**Fig. 1.** (A) Ptychography modulus image of magnetosomes extracted from MV-1 MTB cells. The ptychography data were measured using a photon energy of 708.2 eV, with an image size of  $2 \times 2 \mu\text{m}$  ( $40 \times 40$  points) and a dual-sampling approach where the diffraction pattern was measured at each pixel with both 15- and 150-ms dwell times. A ZP with a 60-nm outer zone width was used. (B) FRC analysis (32) of the image in A. The spatial resolution is 7.2 nm if the 0.5 threshold is used and 6.8 nm if the half-bit threshold is used (beamline 11.0.2).

of part of the magnetosome chains (Fig. S2B). A close examination of the ptychography modulus image shows evidence for some lower density material surrounding the extracted chains (indicated by red arrows in Fig. S2B). The C 1s spectrum of this material (Fig. S3) indicates it is organic and that it has a lipid-like signature, consistent with it being a residue of the lipid membranes that surround magnetosome chains in MTB.

After the ptychography measurement, the same region of this sample was imaged by TEM (Fig. S4). The TEM bright-field image shows a pattern of magnetosomes with identical size, morphology, and orientation as seen in the ptychography modulus image. The TEM also showed that the ptychography measurement had generated a significant build-up of carbon contamination (dark rectangular region in Fig. S4). Further discussion of this signal is given below.

To quantify the spatial resolution of the ptychography images, several methods were used. Fig. 1B presents the calculated

Fourier ring correlation (FRC) (32) of the reconstructed image in Fig. 1A. The FRC curve (blue, Fig. 1B) drops below the chosen threshold line of 0.5 (dashed gray line, Fig. 1B) at a spatial frequency of  $0.147 \text{ nm}^{-1}$ , which corresponds to a spatial resolution of 6.8 nm. A simple 10–90% edge sharpness evaluation gave an estimate of 7 nm (36), whereas a power spectral density method estimated a spatial resolution of 5 nm. A similar resolution was also achieved in Fe  $L_{2,3}$  ptychography studies of  $\text{Li}_x\text{FePO}_4$  crystals (33). A yet higher spatial resolution of 3 nm was reported by Shapiro et al. (32), but that resolution was measured using considerably shorter wavelength X-rays (1,500 eV, 0.85 nm) on a very high-contrast, 1D test pattern.

### Fe 2p Spectro-ptychography Study of Magnetosomes in Whole MV-1 Cells.

Fig. 2 compares the conventional STXM transmission image (Fig. 2A) of multiple MV-1 cells with the ptychography modulus image (Fig. 2B) of the same region. The data were measured at 710 eV (peak around Fe  $L_3$  absorption) using a ZP with a 100-nm outer zone width. Here, the typical morphology of chains of well-resolved individual magnetosomes is observed in the ptychography modulus image, although the magnetosomes are not individually resolved and are barely differentiated from the cell structure in the STXM image due to the low-resolution ZP used (120-nm diffraction-limited resolution). Fig. 3A presents ptychography absorption, and ptychography phase images of the region outlined in red in Fig. 2 at five of the 76 photon energies measured. The ptychography absorption images are obtained by converting the ptychography modulus images to optical density (OD) images using the Lambert–Beer law [ $\text{OD} = -\ln(I/I_0)$ ], where  $I$  is the ptychography modulus intensity and  $I_0$  is the reference signal taken from the ptychography signal in a region unobstructed by the cells (more details are provided in *Materials and Methods, Ptychographic Reconstruction*). Movies of the full ptychography absorption and phase stacks (76 images from 700 to 732 eV) are presented in [Movies S1](#) and [S2](#). Fig. 3B plots the ptychographic phase (green) and absorption spectra (red) over the full photon energy range, and averaged over all of the magnetosomes in one cell (location is shown in *Inset*). The ptychographic absorption spectrum (red in Fig. 3B) corresponds to excitation of Fe 2p electrons to final states dominated by ( $2p^{-1}$ , Fe 3d) configurations. The maximum  $L_3$  ptychographic absorption signal occurs at 709.5 eV, which is in good agreement with

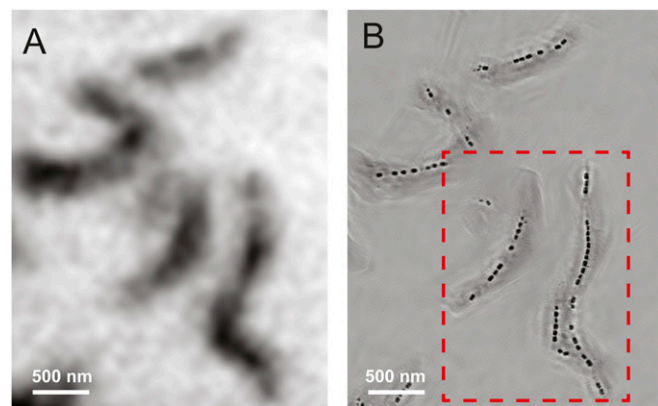


**Fig. 2.** (A) Conventional STXM image of multiple MV-1 cells using a 100-nm outer zone ZP. (B) Ptychography modulus image of the same region. Both images were measured using the Nanosurveyor I instrument on beamline 5.3.2.1. The photon energy was 710 eV. A 100-nm outer zone ZP was used. The STXM image was recorded with  $60 \times 76$  points and a dwell time of 5 ms, whereas the ptychographic data were measured with  $43 \times 50$  points and a dwell time of 300 ms. The red rectangle is the area where the detailed spectro-ptychography stack was measured (beamline 5.3.2.1).

literature reference XAS of magnetite (21–23, 38, 39). The ptychographic phase images (Fig. 3A) show that magnetosomes can be clearly visualized in the phase signal in the pre-edge region (energies below 707 eV) at photon energies where the magnetosomes are barely visible in the ptychographic (or STXM) absorption signal. As the photon energy approaches the absorption peak, magnetosomes become less visible in the phase reconstruction and increase in visibility in the absorption signal. The phase signal is at a minimum at 708.5 eV, and the contrast then inverts after 709.5 eV, as shown in Fig. 3B and [Movie S2](#). Maiden et al. (29) reported the ptychography phase spectrum of  $\text{CoFe}_2\text{O}_4$  in the Fe 2p region and found the minimum phase around the same energy, whereas Shapiro et al. (32) found the minimum in the ptychography phase spectrum at 708.0 eV in  $\text{LiFePO}_4$  and 708.5 eV in  $\text{FePO}_4$ . The ptychography absorption spectrum of magnetosome chains tracks the X-ray absorption spectrum. The significant change in the contrast and morphology in the phase signal several electronvolts below the absorption maximum means that the phase signal might offer advantages in terms of chemical differentiation and mapping. Often, the changes in phase signal across an edge provide more detail, and clearer features than the absorption signal (29, 32), at energies where the X-ray absorption is smaller, which gives advantages with respect to reducing radiation damage. In addition, analysis of the combined phase and absorption signals provides improved chemical contrast, as shown by Shapiro et al. (32).

Fig. 4A displays an average of 76 ptychography OD images of a single MV-1 cell recorded from 700 to 732 eV, in which four different regions (A, B, C, and D) are labeled. Fig. 4B presents the ptychography absorption spectra extracted from these four areas in comparison to reference spectra of Fe(II) and Fe(III) (40). Region A corresponds to a gap between two magnetosome subchains, whose absorption spectrum exhibits a two-peak feature in the  $L_3$  region with the stronger peak at around 708 eV and the weaker one at 710 eV. The reference spectra of Fe(II) and Fe(III) (Fig. 4B) clearly show that Fe(II) species have their main intensity around 708 eV, whereas Fe(III) species have their main intensity around 710 eV (41). The spectrum of the gap region between two magnetosome subchains shows that it consists of both Fe(II) and Fe(III), with the Fe(II) character stronger than the Fe(III) character. Region B represents a region close to one end of a magnetosome chain, where a weak precursor-like structure can be visualized. Similar to the spectrum of region A, the spectrum of region B also has a two-peak feature in the  $L_3$  region, but with an inverted intensity ratio of the 708 eV peak to the 710 eV peak. Although it is challenging to determine quantitatively the amount of Fe(III) and Fe(II) ions in region B, it is evident that there is more Fe(III) in precursor B than in gap area A. Region C corresponds to a single immature magnetosome, whereas region D represents a mature magnetosome. Compared with the spectrum of mature magnetosomes (D), the spectrum of the immature magnetosome (C) is rather different, with a shoulder evident on the low-energy side of the  $L_3$  region, labeled with a red arrow in Fig. 4B, suggesting that these immature magnetosomes might be an  $\text{Fe}_2\text{O}_3$  phase (42). In our previous study, we showed that these immature magnetosomes are nonmagnetic because they have zero XMCD signals (23). In a real-time XMCD study of *Magnetospirillum gryphiswaldense* strain MSR-1, Staniland et al. (11) reported the presence of a surface layer of a nonmagnetic phase, hematite ( $\alpha\text{-Fe}_2\text{O}_3$ ), in immature magnetosomes that is rapidly converted to magnetite in a very short time.

### Ptychographic XMCD Study of Extracellular and Intracellular Magnetosomes.

Fig. 5A presents the ptychographic XMCD absorption signals of an extracellular magnetosome chain measured at 708.2 eV, 709.5 eV, and 710.5 eV. The XMCD signal is generated by taking the difference of two images, one recorded with the photon polarization parallel and the other antiparallel to

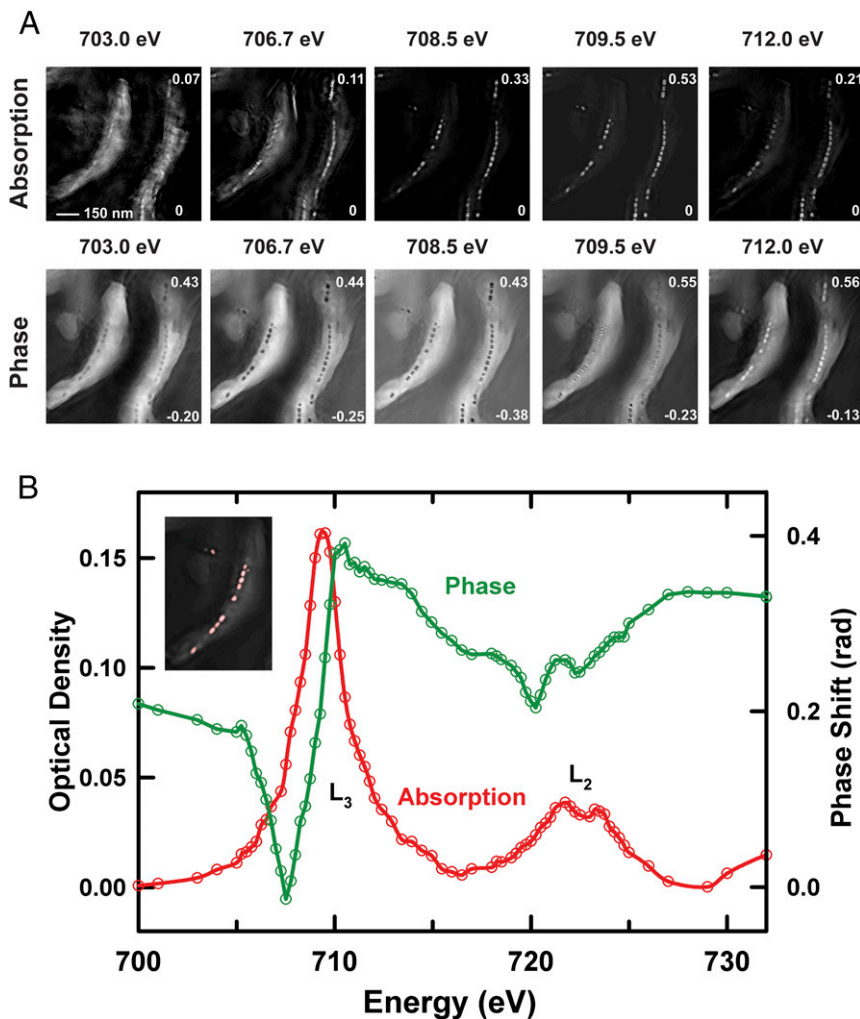


**Fig. 3.** (A) Reconstructed ptychography absorption and ptychography phase images of MV-1 cells at five photon energies: 703.0 eV, 706.7 eV, 708.5 eV, 709.5 eV, and 712.0 eV. (B) Fe  $L_{2,3}$ -edge ptychographic absorption (red) and phase (green) spectra averaged over all of the mature magnetosomes in the MV-1 cells in A. (Inset) Average of all ptychography absorption images in the stack. The region from which the spectra are extracted is indicated in red (beamline 5.3.2.1).

the magnetosome magnetization. A movie of the full ptychographic XMCD absorption stack, ranging from 704 to 716 eV, is shown in [Movie S3](#). Fig. 5B shows the Fe  $L_3$  XAS spectra of the extracellular magnetosome chain recorded with the photon polarization parallel (red) and antiparallel (green) to the sample magnetization, which were extracted from the full sequence of ptychographic absorption images. The corresponding XMCD spectrum (blue), the difference of the two ptychographic absorption spectra (parallel and antiparallel), is also plotted in Fig. 5B. The ptychographic XMCD absorption spectrum of the magnetosomes ( $\text{Fe}_3\text{O}_4$ ) in Fig. 5B has three distinct peaks,  $B_1$  (708.2 eV), A (709.5 eV), and  $B_2$  (710.5 eV), which are mainly associated with Fe(II) in the octahedral site, Fe(III) in the tetrahedral site, and Fe(III) in the octahedral site, respectively (43). In addition, the sign of each of these three peaks is determined by the spin direction (spin up or spin down) of the Fe ions, which is related to antiferromagnetic coupling between the spins on the octahedral and tetrahedral sites (43). As a result, the  $B_1$  and  $B_2$  peaks are negative-going, whereas the A peak is positive-going, leading to systematic contrast changes in the ptychographic XMCD absorption images at the energies of peaks  $B_1$ , A, and  $B_2$ , which show an alternation of contrast at the magnetosomes as the energy increases from 708.2 to 710.5 eV. The extracted magnetosome sample was partly oxidized due to exposure to air over many months. As a re-

sult, the oxidized state of this sample leads to a shoulder at 708.5 eV in the ptychography absorption spectrum and a much stronger  $B_2$  peak in the XMCD absorption spectrum (38).

Fig. 5C presents the ptychographic XMCD phase signals of the extracellular magnetosome chain measured at 708.2 eV, 709.5 eV, and 710.5 eV. A movie of the full ptychographic XMCD phase stack, ranging from 704 to 716 eV, is presented as [Movie S4](#). Fig. 5D shows the Fe  $L_3$  ptychographic phase spectra of the extracellular magnetosome chain recorded with the photon polarization parallel (red) and antiparallel (green) to the sample magnetization, which were extracted from the full sequence of ptychographic phase images. Contrary to the “negative-positive-negative” contrast change of magnetosomes in ptychographic XMCD absorption signals, an almost reversed “positive-negative-positive” contrast change is observed in the ptychographic XMCD phase signals in Fig. 5C. Although the interpretation of ptychography phase spectra is not well established, the phase spectra recorded with the two opposite elliptical polarizations do have different spectral fine structures. More importantly, the ptychographic XMCD phase spectrum in Fig. 5D (blue) derived from the difference of the two ptychographic phase spectra (parallel and antiparallel) also exhibits a three-peak feature in the  $L_3$  region but with an opposite sign to the sign in the ptychographic absorption spectrum in Fig. 5B. In a

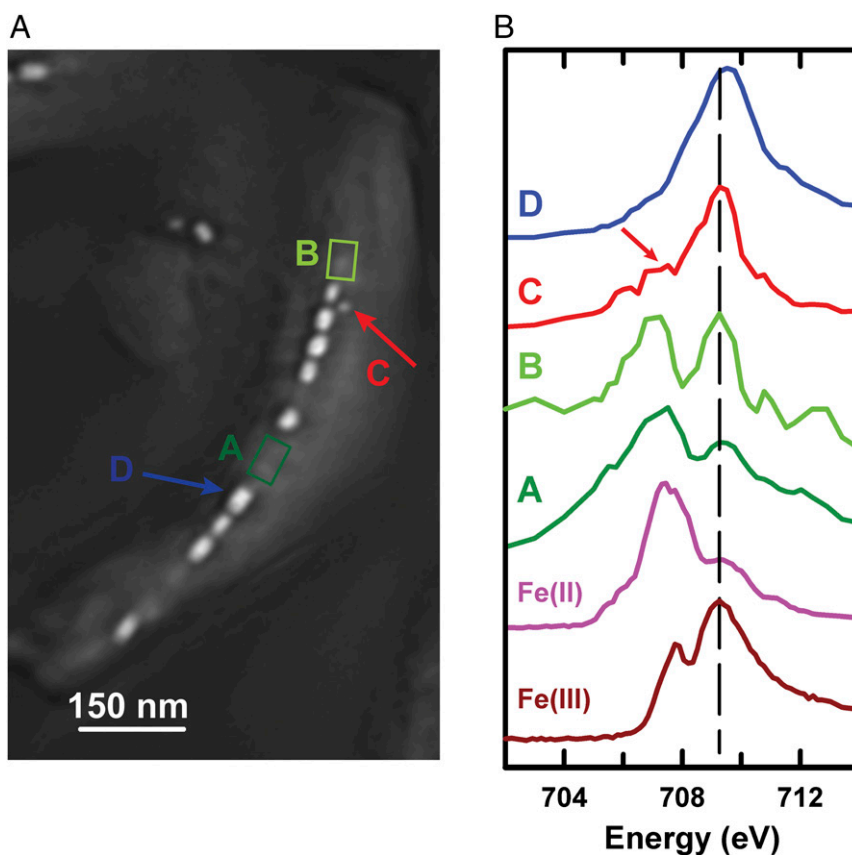


**Fig. 4.** (A) Average of 76 ptychography absorption images of a single MV-1 cell from 700 to 732 eV. Four regions, labeled A, B, C, and D, are identified. (B) Fe  $L_3$  spectra from a gap in the magnetosome chain (region A), a precursor-like region (B), an immature magnetosome (C), and a mature magnetosome (D). The spectra of  $\text{FeCl}_2 \cdot 0.4\text{H}_2\text{O}$  [Fe(II)] and  $\text{FeCl}_3 \cdot 0.6\text{H}_2\text{O}$  [Fe(III)] are also plotted (40) (beamline 5.3.2.1).

previous study, Scherz et al. (44) applied soft X-ray holography to magnetic Co/Pd multilayer samples using left and right circular polarization, and they also observed that the absorption and phase differences had opposite signs in the resonance region. These results indicate that XMCD signals computed from ptychographic phase spectra contain information related to magnetic properties of the sample that can be used to probe site occupancy and magnetic moments of different Fe environments in magnetosomes. In addition, the spectral features in the range of 710–716 eV in the XMCD phase spectrum change more significantly than the spectral features in 708- to 710-eV region. One possible reason might be related to the successive mode used to collect XAS data. In this study, the complete image stacks were first measured with one polarization before an elliptically polarizing undulator reverses the polarization. According to a previous study (22), measurements made using the successive mode are of lower quality and reliability, due to beamline instability and carbon build-up, than concurrent mode measurements, which alternate two opposite polarizations at each energy point.

Fig. 6A compares the XMCD signals of an intracellular MV-1 magnetosome chain, as observed in the ptychography absorption and ptychography phase signals, respectively. These XMCD images were measured at 708.2 eV, 709.5 eV, and 710.5 eV, which correspond to the energies of the XMCD peaks B<sub>1</sub>, A, and B<sub>2</sub>, respectively (Fig. 6B). Movies of the ptychographic XMCD absorption and phase stacks of an intracellular chain measured over the Fe  $L_3$  edge (700–716 eV) are presented as [Movies S5](#) and [S6](#). Conventional STXM OD images of this whole MV-1 cell measured at 710 eV and 700 eV using a ZP with an outer zone width of 60 nm are shown in [Fig. S5](#). Fig. 6B and C presents the

Fe  $L_3$  XAS spectra of the intracellular magnetosome chain recorded with the photon polarization parallel (red) and anti-parallel (green) to the sample magnetization, which were extracted from the full sequence of ptychographic absorption and phase images, respectively. The corresponding XMCD spectra (blue) are also plotted in Fig. 6B and C. The measured XAS and XMCD ptychography absorption spectra are in good agreement with reference XAS and XMCD spectra of magnetosomes recorded in conventional transmission mode (21, 22, 38), suggesting that the magnetic information is retrieved properly with ptychography absorption. As with the ptychographic XMCD absorption signals of the extracellular magnetosome chain (Fig. 5A), the intracellular magnetosome chain exhibits a negative-positive-negative contrast pattern as the energy increases from 708.2 to 710.5 eV (Fig. 6A). However, the ptychography XMCD phase signals in Fig. 6A do not show the alternating contrast change of magnetosomes with increasing energy. In addition, the ptychographic XMCD phase spectrum of the intracellular magnetosome chain is ill-defined in the 708- to 711-eV region (Fig. 6C). This case is in contrast to the case of the extracellular magnetosome chain, where an XMCD phase spectrum with a reversed sign relative to the XMCD absorption spectrum was observed in phase mode (Fig. 5D). Possible reasons for this discrepancy are proposed in *Discussion*.

Reduction of Fe compounds by high doses of soft X-rays is known to occur (45); thus, we need to consider the possibility that the high X-ray doses used to measure the ptychography signals from the whole cell may have changed the chemical state of the Fe in magnetosomes. To check for this possibility, conventional STXM (using a ZP with a 35-nm outer zone) was used

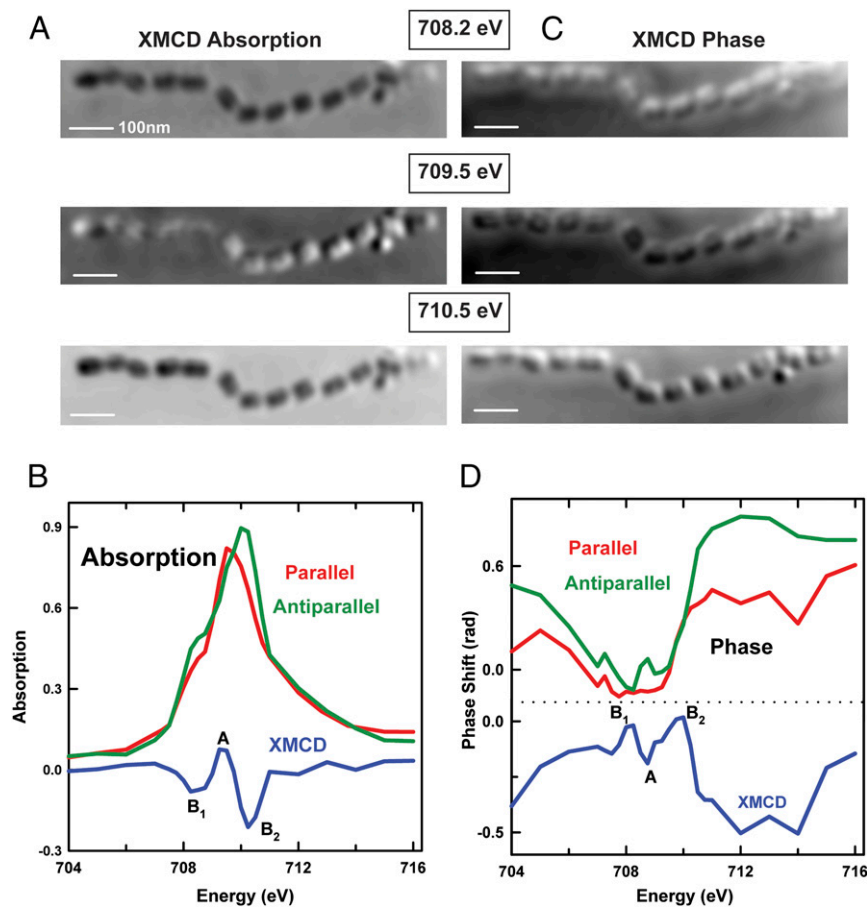


**Fig. 5.** (A) Ptychography absorption XMCD signals (difference of images recorded with parallel and antiparallel 90% circular polarization) from an extracellular magnetosome chain measured at 708.2 eV, 709.5 eV, and 710.5 eV, respectively. The gray-scale range is  $-0.18$  to  $0.18$  OD,  $-0.1$  to  $0.25$  OD, and  $-0.47$  to  $0.15$  OD, respectively. (B) Fe  $L_3$ -edge ptychoabsorption integrated over the extracellular magnetosome chain in A. The XMCD spectrum (blue), the difference of two XAS spectra recorded with photon polarization parallel (red) and antiparallel (green) to sample magnetization, is also plotted in B. (C) Ptychography phase XMCD signals from an extracellular magnetosome chain measured at 708.2 eV, 709.5 eV, and 710.5 eV, respectively. The gray-scale range is  $-0.25$  to  $0.19$  rad,  $-0.22$  to  $0.17$  rad, and  $-0.39$  to  $0.22$  rad, respectively. (D) Fe  $L_3$  ptychographic phase spectra of the extracellular magnetosome chain recorded with the photon polarization parallel (red) and antiparallel (green) to the sample magnetization, which were extracted from the full sequence of ptychographic phase images. The XMCD phase spectrum (blue), the difference of two XAS spectra recorded with photon polarization parallel (red) and antiparallel (green) to sample magnetization, is also plotted in D (beamline 11.0.2).

to measure the Fe  $L_3$  XAS spectrum of the cell that had been studied by ptychography (as shown in Fig. 6), along with the Fe  $L_3$  XAS spectrum of several other cells on the same grid that had not previously been exposed to the X-ray beam. These results are presented in Fig. S6 and discussed in detail in *Supporting Information*. We found that the Fe  $L_3$  spectrum of the magnetosomes in the cell measured by high-dose ptychography was identical to the spectrum measured from four magnetosome chains in multiple MV-1 cells that were not exposed previously to the X-ray beam, indicating that the ptychographic XMCD measurement had a negligible effect on the chemical composition of the magnetosomes. However, the high dose did cause radiation damage to the cellular material in addition to causing carbon build-up over the region scanned in the ptychography measurement. Fig. S7 and accompanying discussion in *Supporting Information* compare the C 1s spectra of the heavily dosed cell with the spectra of adjacent, unexposed cells. As expected, comparison showed that the cell receiving the large dose in the ptychography study was heavily modified with a negligible protein signature and a strong C 1s  $\rightarrow \pi^*$  transition at 285 eV, a signature of partly crystalline graphitic carbon. In contrast, the spectrum of unexposed cells exhibited the expected protein-dominated C 1s spectrum.

## Discussion

The existence of mineral precursors in the process of magnetosome biomineralization in MTB cells has been debated for some time. Using Mössbauer spectroscopy, Frankel et al. (46) reported that an amorphous ferrihydrite [ $(\text{Fe}^{3+})_2\text{O}_3 \cdot 0.5\text{H}_2\text{O}$ ] precursor formed, which was then partially reduced and dehydrated to  $\text{Fe}_3\text{O}_4$ . In contrast, Abe et al. (47) suggested that ferric hydroxyl phases of goethite ( $\alpha\text{-FeOOH}$ ) and lepidocrocite ( $\gamma\text{-FeOOH}$ ) are mineral precursors of  $\text{Fe}_3\text{O}_4$  in a process mimicking bacterial magnetosome synthesis. However, Faivre et al. (48) did not observe any mineral precursor in a time-resolved Mössbauer study and suggested that Fe(II) and Fe(III) quickly coprecipitate to form  $\text{Fe}_3\text{O}_4$  within magnetosome vesicles. Using XAS combined with XMCD techniques, Staniland et al. (11) observed that a nonmagnetic hematite ( $\alpha\text{-Fe}_2\text{O}_3$ ) phase acted as a precursor of  $\text{Fe}_3\text{O}_4$ , which then rapidly converted to mature  $\text{Fe}_3\text{O}_4$  in 15 min. It is notable that an immature magnetosome phase was observed previously using conventional STXM (23). However, characterization by conventional STXM is very challenging, particularly when the ROI is smaller than 10 nm. In this context, localization of mineral precursors and the observation of a single immature magnetosome inside an MV-1 cell (Fig. 4A) show that ptychography

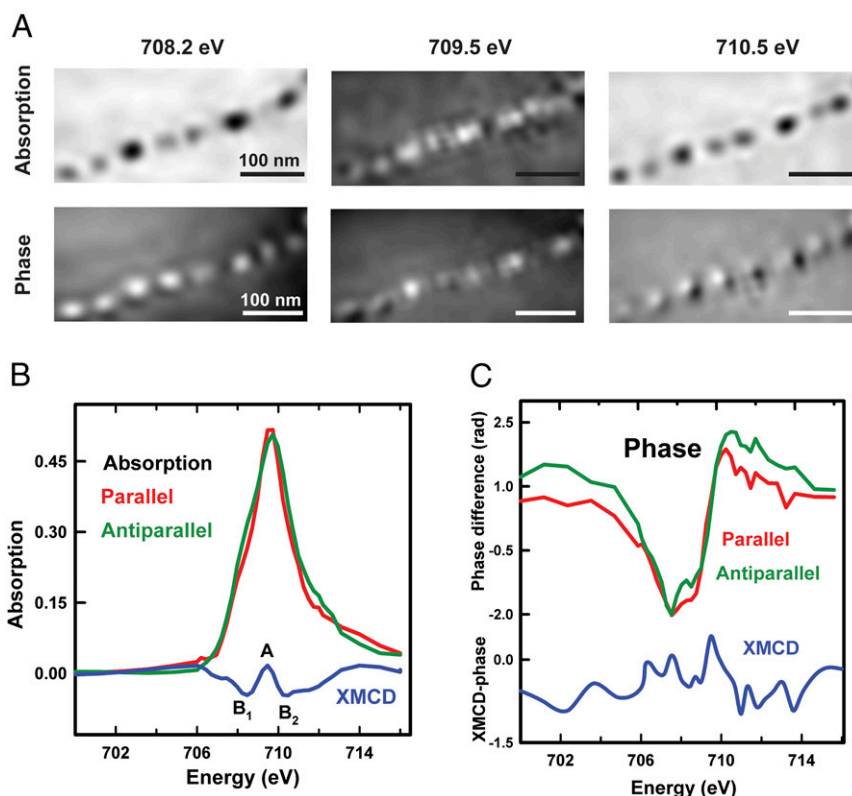


**Fig. 6.** (A) Comparison of the XMCD signal from a single magnetosome chain in an individual MV-1 cell in the reconstructed ptychography absorption and ptychography phase signals, respectively. The XMCD signal was measured at 708.2 eV, 709.5 eV, and 710.5 eV, respectively. Fe  $L_3$ -edge absorption (B) and phase signals (C) of the intracellular magnetosome chain in A are shown. The XMCD spectrum (blue), the difference of two XAS spectra recorded with photon polarization parallel (red) and antiparallel (green) to sample magnetization, is also shown in each panel (beamline 11.0.2).

will be a valuable tool to study the biomineralization process in MTB cells.

Fig. 4B shows that the gap, precursor-like region, immature magnetosome, and mature magnetosome have different Fe  $L_3$  absorption spectra, indicating that different iron species are present in cells of MV-1. These results, and further systematic ptychographic spectroscopy studies as a function of magnetosome development, will provide a better understanding of how these Fe phases are converted and mediated to form  $Fe_3O_4$ . Previous studies have shown that Fe(II) is taken up from the environment and transported into magnetosome vesicles by several types of MTB cells, including *Magnetospirillum magnetotacticum* MS-1 (46), *Ms. gryphiswaldense* MSR-1 (48), and *Magnetospirillum magneticum* AMB-1 (49) strains. In this study, over 70% of the iron in the culture medium used to grow MV-1 cells is Fe(II), so it is assumed that Fe(II) is also the major Fe component that is taken up by cells of MV-1 (4). This assumption is consistent with the result that there is more Fe(II) than Fe(III) in the gap area. However, the fact that the precursor-like region has more Fe(III) than the gap area suggests that Fe(II) is probably oxidized to Fe(III) to form the precursor phase. In addition, it is likely that the precursor is further oxidized to a hematite ( $\alpha$ - $Fe_2O_3$ ) phase in the form of immature magnetosomes (Fig. 4A). The  $\alpha$ - $Fe_2O_3$  may be considered as an intermediate phase before  $Fe_3O_4$  formation, as reported by Staniland et al. (11). Based on these observations, we propose that the pathway of magnetosome biomineralization for *M. blakemorei* strain MV-1 is as follows:

- i) Iron is taken up from the environment as Fe(II) or Fe(III).
- ii) Part of the Fe(II) is then oxidized to Fe(III) to form a precursor, either inside or as the Fe(II) enters the cell.

- iii) The precursor is further oxidized and transformed to  $\alpha$ - $Fe_2O_3$ , which is then ultimately converted to mature  $Fe_3O_4$ .

We have used soft X-ray spectro-ptychography to measure the XAS and XMCD spectra from individual magnetosomes within an individual MTB. By taking advantage of a fast CCD camera and the Nanosurveyor-I instrument at the Advanced Light Source (ALS) 5.3.2.1 beamline (33), Fe 2p XAS spectra (from 700 to 732 eV) were measured in  $\sim 8$  h on multiple MTB cells over an area of  $2.5 \mu m \times 2.5 \mu m$ . This procedure allowed measurement of the full Fe L-edge ptychographic absorption and phase spectra of magnetosomes in whole cells. Previously, other studies showed that chemical differentiation can be achieved through the phase signal derived from ptychographic measurements (29, 50, 51). However, the ptychographic data in those prior studies were only collected at a few discrete energy points so that the full ptychography spectra were missing. Recently, ptychography absorption and phase spectra over the full energy range of an absorption edge have been obtained (32, 33). In this study, the ptychographic scan spanned from 700 to 732 eV with 76 points, which provided a detailed comparison of the absorption and phase signal over the full range of the Fe  $L_{2,3}$  absorption and phase spectrum. The phase signal exhibited inverted contrast compared with the modulus signal in the pre-edge region but reversed its sign after the absorption edge (Fig. 3). Because the phase signal changes more significantly than modulus signals through the absorption resonance, it might possess unique advantages over the absorption signal in terms of chemical differentiation, especially around absorption resonances. Using the high brightness and 90% circularly polarized light in the 11.0.2 undulator beamline at the ALS, we measured Fe  $L_3$  XMCD spectra from both extracellular and intracellular magnetosomes.

We showed that XMCD spectra could be derived from both isolated and intracellular magnetosomes, and that the ptychography absorption spectrum is in good agreement with X-ray absorption reference spectra (21–23). The ptychographic XMCD phase spectrum was measured from magnetosomes extracted from cells, and exhibited a negative-positive-negative feature from 708 to 712 eV, similar to the absorption and ptychographic modulus. However, the phase signal from intracellular magnetosomes differed. We speculate this difference may be due to the presence of surrounding poorly crystallized biomaterials that affect the phase. The results clearly indicate that both absorption and phase ptychography signal can probe magnetic dichroic information.

It is of interest to consider radiation damage in these types of measurements. Clearly, the doses used for ptychography are such that the biological components of these samples are extremely modified (Fig. S7). However, as shown in the follow-up study (Fig. S6), the ptychography dose was not sufficient to modify the Fe L<sub>3</sub> spectrum. The lower radiation sensitivity of the Fe L<sub>3</sub> spectrum allowed for the detailed intracellular results presented in Fig. 4. In general, the biological components of MTB cells can be studied without significant radiation damage, albeit at lower spatial resolution, using conventional STXM, as shown in many studies of biological and environmental samples (22, 52–55). With present soft X-ray ptychography capabilities, the doses required are such that the C 1s, N 1s, and O 1s spectra, which are those spectra most sensitive to the biological components, cannot be measured without damage. With improvements in the sensitivity and reduced backgrounds of ptychography cameras, better acquisition strategies, and improved reconstruction algorithms, there is hope that at least some biological and other soft matter systems can be investigated with spectro-ptychography. Operation under cryogenic conditions will likely help preserve the morphology of the soft matter components to higher doses but will likely have little influence on the rate of spectral transformations caused by radiation damage (56). We note that TEM is also very much challenged by radiation damage, yet significant improvements in the efficiency of column optics and detectors, as well as improved acquisition strategies, have been made in recent years, and these improvements are allowing increasingly effective studies of soft matter. In a recent work, Suzuki et al. (57) used a combination of ptychography and in-line holography with 6.5-keV radiation to image MTB. This dark-field ptychography method demonstrated a spatial resolution of 15 nm on high-contrast test patterns, and individual magnetosomes were resolved in the images of whole MO-1 cells (as 300- to 400-nm thick dried cells). However, spectroscopic information was not obtained, and the estimated dose ( $2 \times 10^9$  Gy) was at least an order of magnitude larger than the dose we estimate was used for the full spectroscopic study in this work.

## Summary

In this work, we applied spectro-ptychography at the Fe L<sub>3</sub> edge to study magnetosomes from the MTB *M. blakemorei* strain MV-1, both extracted and intracellularly. The Fe L<sub>3</sub> XAS and XMCD spectra of individual magnetosomes were obtained with the ptychographic modulus and phase mode. A spatial resolution of 7 nm was achieved in this work. To the best of our knowledge, this spatial resolution is the highest spatial resolution obtained so far for soft X-ray imaging below 1 keV. Spectro-ptychography, which combines high spatial resolution and chemical sensitivity, is a promising probe for future biomineralization studies.

## Materials and Methods

**Sample Preparation.** Cells of *M. blakemorei* strain MV-1 were cultured anaerobically in liquid cultures as described by Dean and Bazylinski (58). Magnetosomes were extracted from MV-1 cells using the procedure developed by Alphandéry et al. (37).

**Experimental Methods.** STXM measurements were made at beamlines 11.0.2 and 5.3.2.1 at the ALS at the Lawrence Berkeley National Laboratory (LBNL) and at beamline 10ID1 at the Canadian Light Source. In STXM, a ZP with a narrow outer zone width (typically 25 nm) is used to focus monochromated X-rays to an ~30-nm spot, and images are recorded by *x-y* raster scanning of the sample, which is positioned at the focus of the ZP. The ZPs used in this work were provided by the Centre for X-Ray Optics (LBNL), whose ZPs have achieved the world record spatial resolution for direct 2D imaging in both full-field and scanning transmission microscopy (59). We note in passing that ZPs have also been used as focusing optics in hard X-ray microscopes (60) and for monochromatization of femtosecond pulses in extreme UV light (61); thus, they are an essential aspect of modern X-ray science.

Ptychographic measurements were carried out using the 5.3.2.1 bending magnet and 11.0.2 undulator beamlines at the ALS, LBNL. Because a larger spot size with uniform and highly coherent illumination is desirable in ptychography, low-resolution ZPs with outer zone widths of 60 nm (beamline 11.0.2) and 100 nm (beamline 5.3.2.1) were used to produce a focused X-ray spot with high intensity and high coherence. The ptychographic results shown in Figs. 1, 4, and 5 were measured with the STXM on beamline 11.0.2, whereas the ptychographic results shown in Figs. 2 and 3 were measured using the Nanosurveyor I instrument at beamline 5.3.2.1. At beamline 11.0.2, a Princeton Instruments direct-sense X-ray camera was used for data collection. The sample was scanned in focus with a step size of 50 nm. A double-exposure mode that combined a short exposure (15 ms) and a long exposure (150 ms) was used at beamline 11.0.2 to extend the dynamic range as described by Shapiro et al. (32). At beamline 5.3.2.1, the sample was scanned in focus with a step size of 70 nm. A custom, high-frame-rate CCD detector, developed at the LBNL and Brookhaven National Laboratory (BNL) was used to record the diffraction data. At beamline 5.3.2.1, a single exposure time of 200 ms was used and a partially transmitting silicon beam stop was used to increase dynamic range. In both systems, the incoherent background signal was measured with the same CCD settings and the beamline shutter closed. This background was then subtracted in the data processing.

**Ptychographic Reconstruction.** The ptychography reconstruction provides a complex valued result, where the real part is related to elastic scattering and the imaginary part is related to absorption (34). If we denote the exit wave reconstructed with ptychography as *P*, then the OD can be calculated as:

$$OD = -\ln(|P|/|P_0|),$$

where *P*<sub>0</sub> is the signal in the reconstruction in a region unobstructed by the sample, or from a measurement in a featureless region containing nonsample components, measured under the same instrumental conditions (ZP, incident flux, sampling time, camera settings, etc.) and reconstructed in exactly the same way. In this study, we refer to this result as ptychography absorption.

The wave function *P* can be divided into a real part (Re[*P*]) and an imaginary part (Im[*P*]). Then, a relative phase term  $\phi$ , referred to as the ptychography phase in this study, can be calculated as:

$$\phi = \arctan(\text{Im}[P]/\text{Re}[P]) - \arctan(\text{Im}[P_0]/\text{Re}[P_0]).$$

The measured ptychography images were reconstructed using 200 iterations of the relaxed averaged alternating reflection (RAAR) algorithm implemented in the SHARP Center for Applied Mathematics for Energy Research Applications ptychography code (62, 63). Illumination and incoherent background refinements were used in every other iteration.

**Image and Spectral Analysis.** Individual ptychography modulus and ptychography phase images were assembled into stacks and analyzed in aXis2000 (64). The stacks were aligned using Fourier correlation methods. A threshold masking procedure was used to establish ROIs, including individual and chains of magnetosomes, as well as intracellular regions. These ROI masks were then applied to the ptychography stacks to generate XAS and XMCD spectra. The ptychography modulus and STXM transmission signals were converted to OD signals using the intensity through an area free of iron and off the cell or extracted magnetosomes but close to the region under study.

**ACKNOWLEDGMENTS.** We thank Dr. Chunpeng Wang (Shanghai Institute of Applied Physics) for his spatial resolution analysis with the power spectral density method. Some scanning transmission X-ray microscope (STXM) results were measured at the STXM on beamline 10ID1 at the Canadian Light Source, which is supported by the Canada Foundation for Innovation, Natural Sciences and Engineering Research Council (NSERC), the Canadian

Institute for Health Research, the National Research Council, and University of Saskatchewan. This research was funded by the NSERC and Canada Research Chairs. Most measurements were made at the 5.3.2.1 and 11.0.2 beamlines at the ALS, which is supported by the Division of Basic Energy Sciences of the US Department of Energy under Contract DE-AC02-05CH11231. This

work is also partially supported by the Center for Applied Mathematics for Energy Research Applications, which is a partnership between Basic Energy Sciences and Advanced Scientific Computing Research at the US Department of Energy. D.A.B. is supported by US National Science Foundation Grant EAR-1423939.

- Nazaries L, et al. (2013) Evidence of microbial regulation of biogeochemical cycles from a study on methane flux and land use change. *Appl Environ Microbiol* 79(13): 4031–4040.
- Ehrlich HL (1998) Geomicrobiology: Its significance for geology. *Earth Sci Rev* 45(1-2): 45–60.
- Gargaud M, Lopez-Garcia P, Martin H (2011) *Origins and Evolution of life, An Astrobiological Perspective* (Cambridge Univ Press, Cambridge, UK).
- Bazylinski DA, Frankel RB (2004) Magnetosome formation in prokaryotes. *Nat Rev Microbiol* 2(3):217–230.
- Uebe R, Schüler D (2016) Magnetosome biogenesis in magnetotactic bacteria. *Nat Rev Microbiol* 14(10):621–637.
- de Araujo FF, Pires MA, Frankel RB, Bicudo CEM (1986) Magnetite and magnetotaxis in algae. *Biophys J* 50(2):375–378.
- Mann S, Sparks NH, Walker MM, Kirschvink JL (1988) Ultrastructure, morphology and organization of biogenic magnetite from sockeye salmon, *Oncorhynchus nerka*: Implications for magnetoreception. *J Exp Biol* 140:35–49.
- Maher BA (1998) Magnetite biomineralization in termites. *Proc Biol Sci* 265(1397): 733–737.
- Wiltshcko W, Wiltshcko R (2005) Magnetic orientation and magnetoreception in birds and other animals. *J Comp Physiol A Neuroethol Sens Neural Behav Physiol* 191(8): 675–693.
- Kirschvink JL, Kobayashi-Kirschvink A, Woodford BJ (1992) Magnetite biomineralization in the human brain. *Proc Natl Acad Sci USA* 89(16):7683–7687.
- Staniland S, Ward B, Harrison A, van der Laan G, Telling N (2007) Rapid magnetosome formation shown by real-time x-ray magnetic circular dichroism. *Proc Natl Acad Sci USA* 104(49):19524–19528.
- Komeili A (2012) Molecular mechanisms of compartmentalization and biomineralization in magnetotactic bacteria. *FEMS Microbiol Rev* 36(1):232–255.
- Qian L (2013) Quantitative magnetic characterization of single cells. PhD dissertation (Stanford University, Stanford, CA).
- Amemiya Y, Tanaka T, Yoza B, Matsunaga T (2005) Novel detection system for biocolloids using nano-sized bacterial magnetic particles and magnetic force microscopy. *J Biotechnol* 120(3):308–314.
- Dunin-Borkowski RE, et al. (1998) Magnetic microstructure of magnetotactic bacteria by electron holography. *Science* 282(5395):1868–1870.
- Sievers S, et al. (2012) Quantitative measurement of the magnetic moment of individual magnetic nanoparticles by magnetic force microscopy. *Small* 8(17):2675–2679.
- Freeman MR, Choi BC (2001) Advances in magnetic microscopy. *Science* 294(5546): 1484–1488.
- Dunin-Borkowski RE, et al. (2001) Off-axis electron holography of magnetotactic bacteria: magnetic microstructure of strains MV-1 and MS-1. *Eur J Mineral* 13(4): 671–684.
- Stöhr J, Siegmann HC (2006) *Magnetism: From Fundamentals to Nanoscale Dynamics* (Springer, Berlin).
- Hitchcock AP (2012) Soft X-ray imaging and spectromicroscopy. *Handbook of Nanospectroscopy*, eds Tendeloo GV, Dyck DV, Pennycook SJ (Wiley VCH Press, Weinheim, Germany), pp 745–791.
- Lam KP, et al. (2010) Characterizing magnetism of individual magnetosomes by X-ray magnetic circular dichroism in a scanning transmission X-ray microscope. *Chem Geol* 270(1-4):110–116.
- Kalirai SS, et al. (2012) Examining the chemistry and magnetism of magnetotactic bacterium *Candidatus Magnetovibrio blakemorei* strain MV-1 using scanning transmission X-ray microscopy. *Chem Geol* 300:301:14–23.
- Kalirai SS, Bazylinski DA, Hitchcock AP (2013) Anomalous magnetic orientations of magnetosome chains in a magnetotactic bacterium: *Magnetovibrio blakemorei* strain MV-1. *PLoS One* 8(1):e53368.
- Coker VS, et al. (2012) Characterisation of the dissimilatory reduction of Fe(III)-oxyhydroxide at the microbe-mineral interface: The application of STXM-XMCD. *Geobiology* 10(4):347–354.
- Thibault P, Guizar-Sicairos M, Menzel A (2014) Coherent imaging at the diffraction limit. *J Synchrotron Radiat* 21(Pt 5):1011–1018.
- Thibault P, et al. (2008) High-resolution scanning x-ray diffraction microscopy. *Science* 321(5887):379–382.
- Edo TB, et al. (2013) Sampling in x-ray ptychography. *Phys Rev A* 87(5):1–8.
- Giewekemeyer K, et al. (2010) Quantitative biological imaging by ptychographic x-ray diffraction microscopy. *Proc Natl Acad Sci USA* 107(2):529–534.
- Maiden AM, Morrison GR, Kaulich B, Gianoncelli A, Rodenburg JM (2013) Soft X-ray spectromicroscopy using ptychography with randomly phased illumination. *Nat Commun* 4:1669.
- Tripathi A, et al. (2011) Dichroic coherent diffractive imaging. *Proc Natl Acad Sci USA* 108(33):13393–13398.
- Holler M, et al. (2014) X-ray ptychographic computed tomography at 16 nm isotropic 3D resolution. *Sci Rep* 4:3857.
- Shapiro DA, et al. (2014) Chemical composition mapping with nanometre resolution by soft X-ray microscopy. *Nat Photonics* 8(10):765–769.
- Yu YS, et al. (2015) Dependence on crystal size of the nanoscale chemical phase distribution and fracture in  $\text{Li}_x\text{FePO}_4$ . *Nano Lett* 15(7):4282–4288.
- Rodenburg JM (2008) Ptychography and related diffractive imaging methods. *Adv Imaging Electron Phys* 150(07):87–184.
- Shi X, et al. (2016) Soft x-ray ptychography studies of nanoscale magnetic and structural correlations in thin  $\text{SmCo}_5$  films. *Appl Phys Lett* 108(9):094103.
- Zhu X, et al. (2016) Magnetic studies of magnetotactic bacteria by soft x-ray STXM and ptychography. *AIP Conf Proc* 1696:020002.
- Alphandéry E, et al. (2009) Assemblies of aligned magnetotactic bacteria and extracted magnetosomes: What is the main factor responsible for the magnetic anisotropy? *ACS Nano* 3(6):1539–1547.
- Zhu X, Kalirai SS, Hitchcock AP, Bazylinski DA (2015) What is the correct  $\text{Fe}_{L_{2,3}}$  X-ray absorption spectrum of magnetite? *J Electron Spectroscop Relat Phenom* 199:19–26.
- Goering EJ, Lafkioti M, Gold S, Schuetz G (2007) Absorption spectroscopy and XMCD at the Verwey transition of  $\text{Fe}_3\text{O}_4$ . *J Magn Magn Mater* 310(2):249–251.
- Nagasaka M, et al. (2013) Electrochemical reaction of aqueous iron sulfate solutions studied by Fe L-edge soft X-ray absorption spectroscopy. *J Phys Chem C* 117(32): 16343–16348.
- Chueh WC, et al. (2013) Intercalation pathway in many-particle  $\text{LiFePO}_4$  electrode revealed by nanoscale state-of-charge mapping. *Nano Lett* 13(3):866–872.
- Kim DH, et al. (2009) Interface electronic structures of  $\text{BaTiO}_3/\text{X}$  nanoparticles ( $\text{X} = \gamma\text{-Fe}_2\text{O}_3$ ,  $\text{Fe}_3\text{O}_4$ ,  $\alpha\text{-Fe}_2\text{O}_3$ , and Fe) investigated by XAS and XMCD. *Phys Rev B* 79: 033402.
- Kuiper P, et al. (1997)  $\text{Fe}_{L_{2,3}}$  linear and circular magnetic dichroism of  $\text{Fe}_3\text{O}_4$ . *J Electron Spectroscop Relat Phenom* 86(1-3):107–113.
- Scherz A, et al. (2007) Phase imaging of magnetic nanostructures using resonant soft x-ray holography. *Phys Rev B* 76(21):1–5.
- Schmidt N, et al. (2010) Microspectroscopic analysis of the X-ray-induced photoreduction in Fe- and Mn-containing SMMs. *Z Naturforsch* 65b:390–398.
- Frankel RB, Papaefthymiou GC, Blakemore RP, O'Brien W (1983)  $\text{Fe}_3\text{O}_4$  precipitation in magnetotactic bacteria. *Biochim Biophys Acta* 763:147–159.
- Abe M, Ishihara T, Kitamoto Y (1999) Magnetite film growth at 30 degrees C on organic monomolecular layer, mimicking bacterial magnetosome synthesis. *J Appl Phys* 85(8):5705–5707.
- Faivre D, Böttger LH, Matzanke BF, Schüler D (2007) Intracellular magnetite biomineralization in bacteria proceeds by a distinct pathway involving membrane-bound ferritin and an iron(II) species. *Angew Chem Int Ed Engl* 46(44):8495–8499.
- Nakamura C, Burgess JG, Sode K, Matsunaga T (1995) An iron-regulated gene, magA, encoding an iron transport protein of *Magnetospirillum* sp. strain AMB-1. *J Biol Chem* 270(47):28392–28396.
- Beckers M, et al. (2011) Chemical contrast in soft x-ray ptychography. *Phys Rev Lett* 107(20):208101.
- Takahashi Y, et al. (2011) Multiscale element mapping of buried structures by ptychographic x-ray diffraction microscopy using anomalous scattering. *Appl Phys Lett* 99(13):5–8.
- Schmid G, et al. (2014) Synchrotron-based chemical nano-tomography of microbial cell-mineral aggregates in their natural, hydrated state. *Microsc Microanal* 20(2): 531–536.
- Neu TR, et al. (2010) Advanced imaging techniques for assessment of structure, composition and function in biofilm systems. *FEMS Microbiol Ecol* 72(1):1–21.
- Norlund KL, et al. (2009) Microbial architecture of environmental sulfur processes: A novel syntrophic sulfur-metabolizing consortia. *Environ Sci Technol* 43(23):8781–8786.
- Sedlmair J (2011) *Soft X-Ray Spectromicroscopy of Environmental and Biological Samples* (Univ of Gottingen Press, Gottingen, Germany).
- Beetz T, Jacobsen C (2003) Soft X-ray radiation-damage studies in PMMA using a cryo-STXM. *J Synchrotron Radiat* 10(Pt 3):280–283.
- Suzuki A, Shimomura K, Hirose M, Burdet N, Takahashi Y (2016) Dark-field X-ray ptychography: Towards high-resolution imaging of thick and unstained biological specimens. *Sci Rep* 6:35060.
- Dean AJ, Bazylinski DA (1999) Genome analysis of several marine, magnetotactic bacterial strains by pulsed-field gel electrophoresis. *Curr Microbiol* 39(4):219–225.
- Chao W, et al. (2012) Real space soft x-ray imaging at 10 nm spatial resolution. *Opt Express* 20(9):9777–9783.
- Mayer M, et al. (2013) Efficient focusing of 8 keV X-rays with multilayer Fresnel zone plates fabricated by atomic layer deposition and focused ion beam milling. *J Synchrotron Radiat* 20(Pt 3):433–440.
- Metje J, et al. (2014) Monochromatization of femtosecond XUV light pulses with the use of reflection zone plates. *Opt Express* 22(9):10747–10760.
- Luke DR (2004) Relaxed averaged alternating reflections for diffraction imaging. *Inverse Probl* 37:13.
- Marchesini S, et al. (2016) SHARP: A distributed GPU-based ptychographic solver. *J Appl Crystallogr* 49(4):1245–1252.
- Hitchcock AP (2016) aXis 2000—Analysis of X-ray Images and Spectra. Available at [unicom.mcmaster.ca/aXis2000.html](http://unicom.mcmaster.ca/aXis2000.html). Accessed October 10, 2016.